ARTICLE IN PRESS

Physica B xxx (xxxx) xxx

Contents lists available at ScienceDirect

Physica B: Physics of Condensed Matter

journal homepage: http://www.elsevier.com/locate/physb

# Structural, magnetic and electrical properties of CoSi ferrites synthesized by sol-gel self-propagating method

Zheng-Xiong Tao, Le-Zhong Li *, Xiao-Hui Wu, Xiao-Xi Zhong, Zi-Chen Zhong

*Sichuan Province Key Laboratory of Information Materials and Devices Application, College of Optoelectronic Engineering, Chengdu University of Information Technology, Chengdu, 610225, Sichuan, People's Republic of China*

ARTICLE INFO

*Keywords:*
Co ferrites
Si substitution
Electromagnetic properties

ABSTRACT

$CoFe_2O_4$ is mainly used in magnetic strain sensor, magnetic resonance imaging, supercapacitor, cryogen, high density magnetic recording medium and magneto-optical devices and so on. In this study, $Si_xCo_{1-x}Fe_2O_4$ (where $x = 0$, 0.05, 0.10, 0.15, 0.30, 0.40, 0.50) ferrites were prepared by sol-gel self-propagating method, and the effects of different amount of silicon substitution on the properties of cobalt ferrite were studied. The X-ray diffraction spectrums demonstrate that the secondary phase $Fe_2O_3$, $Fe_{2.56}Si_{0.44}O_4$ and FeO appear when $x \geq 0.15$. The SEM images of the samples show that with the increase of silicon ion content, the porosity of cobalt ferrite increases and the sintering density decreases. The substitution of silicon significantly changed the electromagnetic properties of Co ferrite samples. Fortunately, the coercive force ($H_c$) increased. Moreover, the dielectric constant raised initially when $0 \leq x \leq 0.30$ and then reduced when $0.30 < x \leq 0.50$ with the increasing Si substitution at low frequency, which achieves the maximum at $x = 0.30$.

## 1. Introduction

As a permanent magnet material, cobalt ferrite has been widely studied for its high Curie temperature, high coercivity, high resistivity, high magnetocrystalline anisotropy, medium saturated magnetization, excellent chemical stability as well as good mechanical and thermal solidity [1–6]. This ferrite is mainly used in magnetic strain sensor, magnetic resonance imaging, supercapacitor, cryogen, high density magnetic recording medium and magneto-optical devices and so on [7–11]. In recent years, with the rapid improvement of software and hardware technology in the world, the properties of present materials is difficult to fulfill the needs of the development of electronic equipment, so it is urgent to improve the electromagnetic properties of existing materials to make up for the defects of current materials. Researchers found that metal cation substitution can effectively enhance the electromagnetic properties of ferrites. In many methods of preparing ferrite nanopowders, sol-gel method can produce nanopowders with high purity at lower temperature, and its cost is low [12,13]. Therefore, we prepared the silicon substituted $CoFe_2O_4$ by Sol-gel self-propagating method to improve the electrical and magnetic properties of the material.

As everyone knows, the chemical formula of spinel ferrite is $MeFe_2O_4$, where Me is a divalent cationic metals, like Ni, Zn, Mn, Co, Cu [14–19]. Co ferrite has an inverse spinel structure, and the degree of reversal is decided by the heat-treat condition [20]. Moreover, $Co^{2+}$ is mainly distributed in B sites, $Fe^{3+}$ occupied A (tetrahedral) and B (octahedral) positions, and the number of $Fe^{3+}$ in A positions is almost the same as that in B sites [21]. Generally speaking, the performance of spinel ferrite is mainly decided by the inherent cation occupation between A and B sites, the lattice strain caused by substitution/doping and the properties of substitution/doping elements [1,14]. $CoFe_2O_4$ is anti-spinel structure [11]. Therefore, scientists often use different metal cations substitution to improve the microstructure and electromagnetic properties of cobalt ferrite. In recent years, there are two main types of substitution studies, one is single cation substitution, such as Ni-substituted Co–Mn ferrite [1], Ni-substituted Co ferrite [22], In-substituted $NiFe_2O_4$ ferrite [23], Co replace Fe in $CoFe_2O_4$ [24], Al substituted for Fe in $NiFe_2O_4$ ferrite [19]. And the other is the joint substitution of bimetallic cations, such as the joint substitution of $Si^{4+}$ and $Co^{2+}$ for $Fe^{3+}$ [18], the joint substitution of $Ge^{4+}$ and $Co^{2+}$ for $Fe^{3+}$ [25], the joint substitution of $Ti^{4+}$ and $Co^{2+}$ for $Fe^{3+}$ [21].

Some studies have shown that the addition of different silicon content to ferrite samples will cause different changes in its electrical or magnetic properties [17,26,27]. In addition, $Si^{4+}$ and $Ge^{4+}$ are both

* Corresponding author.
*E-mail address:* lezhongli@cuit.edu.cn (L.-Z. Li).

https://doi.org/10.1016/j.physb.2020.412655
Received 13 August 2020; Received in revised form 19 October 2020; Accepted 20 October 2020
Available online 5 November 2020

tetravalent ions, and the behavior of semiconductors is quite similar. Both $Si^{4+}$ and $Ge^{4+}$ tend to occupy A (tetrahedral) positions in spinel ferrite [18,25,28]. The study of $Ge^{4+}$ substituted cobalt ferrite has been reported [29], but no one has ever done the study of $Si^{4+}$ substituted $Co^{2+}$ for $CoFe_2O_4$ ferrite. Therefore, for the purpose of researching how different $Si^{4+}$ content affects the microstructure and physical performance of $CoFe_2O_4$ ferrite, we produced Si displaced Co ferrite by sol-gel self-propagating method. Subsequently, the microstructure and electromagnetic properties of these samples were tested.

## 2. Experimental process

### 2.1. Production of silicon substituted Co ferrite

The sample of $Si_xCo_{1-x}Fe_2O_4$ (where $x$ = 0, 0.05, 0.10, 0.15, 0.30, 0.40 and 0.50) ferrite nanoparticles were prepared by means of sol-gel self-propagation method. The raw materials used are $Co(NO_3)_2{\cdot}6H_2O$, $Fe(NO_3)_3{\cdot}9H_2O$, Silica powder and citric acid. The molar ratio of citric acid to cation is 3:1. The raw materials were dissolved in a beaker with deionized water and heated to 80 °C in a water bath. So, 500 ml of 0.1 mol/L mixed solution was prepared. The sol precursor was formed after stirring in water bath for 3 h. After mixing, slowly add ammonia to the solution when it cools to normal atmospheric temperature so that regulate the pH to 7. The sol precursor was dried at 80 °C to obtain xerogel. Finally, a small amount of ethanol was poured in as a combustion supporting agent to ignite the xerogel. Then, the self-propagation combustion was used to obtain ferrite nanopowders. Adding a small amount of 7 *wt*% poly-vinylalcohol (PVA) to the prepared ferrite nano powder to grind it into particles. The final sample is obtained by pressing the powder particles into a round piece and sintering in muffle furnace for 4 h at 1050 °C. Table 1 list the chemical reagents dosage used in this experiment.

### 2.2. Structure and performance measurement

The main crystal phase and impurity phase were determined by DX 2700 X-ray diffraction instrument (XRD) (Cu target, $K_\alpha$ irradiation, $\lambda$ = 1.5406 Å) at normal atmospheric temperature. The microstructure of the cross section of the sample was surveyed by the JEOL JSM-6490L scanning electron microscope (SEM). The hysteresis loop of the sample was measured by a Lake Shore 8604 vibrating sample magnetometer (VSM) at normal atmospheric temperature. The dielectric constant ($\varepsilon'$) of the sample at normal atmospheric temperature was measured with WK 6500P LCR meter bridge in the frequency scale from 100 Hz to 1 MHz. The impedance temperature spectrum of the samples from 30 °C to 300 °C was measured by high temperature impedance analyzer.

### 2.3. Formulas

The cell parameter ($a$) of the samples is computed using the following calculation formula [30]:

$$a = \frac{d_{hkl}}{\sqrt{h^2 + k^2 + l^2}} \tag{1}$$

**Table 1**
Dosage of chemical reagent.

| $Si_xCo_{1-x}Fe_2O_4$ | Si (mol) | $Co(NO_3)_2{\cdot}6H_2O$ (mol) | $Fe(NO_3)_3{\cdot}9H_2O$ (mol) | $C_6H_8O_7{\cdot}H_2O$ (mol) |
|---|---|---|---|---|
| $x$ = 0.00 | 0 | 0.05 | 0.1 | 0.45 |
| $x$ = 0.05 | 0.0025 | 0.0475 | 0.1 | 0.45 |
| $x$ = 0.10 | 0.005 | 0.045 | 0.1 | 0.45 |
| $x$ = 0.15 | 0.0075 | 0.0425 | 0.1 | 0.45 |
| $x$ = 0.30 | 0.015 | 0.035 | 0.1 | 0.45 |
| $x$ = 0.40 | 0.02 | 0.03 | 0.1 | 0.45 |
| $x$ = 0.50 | 0.025 | 0.025 | 0.1 | 0.45 |

$h$ $k$ and $l$ are the Miller indices and $d_{hkl}$ is the inter-planar spacing in this calculation formula.

The X-ray density can be counted by the following calculation formula [31,32]:

$$d_x = \frac{8M_m}{N_A a^3} \tag{2}$$

where $M_m$ is the relative molecular mass; $N_A$ is the Avogadro's number and $a$ is the lattice constant.

In addition, the sintering density ($d$) was measured by Archimedes drainage method, and the porosity percentage ($P$) was computed on the basis of the formula:

$$P = \left[1 - \frac{d}{d_x}\right] \times 100\% \tag{3}$$

According to Brown's relation coercive force ($H_c$) combined with anisotropy constant ($K_1$) and saturated magnetization ($M_s$) though the following computed fomula [31]:

$$H_c = \frac{2K_1}{\mu_0 M_S} \tag{4}$$

The real part of the permittivity is calculated from the measured capacitance data according to the following formula [33]:

$$\varepsilon' = \frac{Cd}{\varepsilon_0 A} \tag{5}$$

Here, $C$ is capacitance, $d$ is the thick of the pellet, $\varepsilon_0$ is the vacuum dielectric constant, A is the circular area of the sample.

The saturation magnetization of cubic spinel ferrite can be calculated by the following formula [34]:

$$M_s = \frac{8M}{a^3} \tag{6}$$

$$M = |M_B - M_A| \tag{7}$$

where $M_A$, $M_B$ are the magnetization of A and B atoms, respectively, $a$ is lattice constant and $M$ is the net magnetic moment.

## 3. Results and analysis

### 3.1. Microstructure properties

The XRD diffraction spectrums of $Si_xCo_{1-x}Fe_2O_4$ ($x$ = 0, 0.05, 0.10,

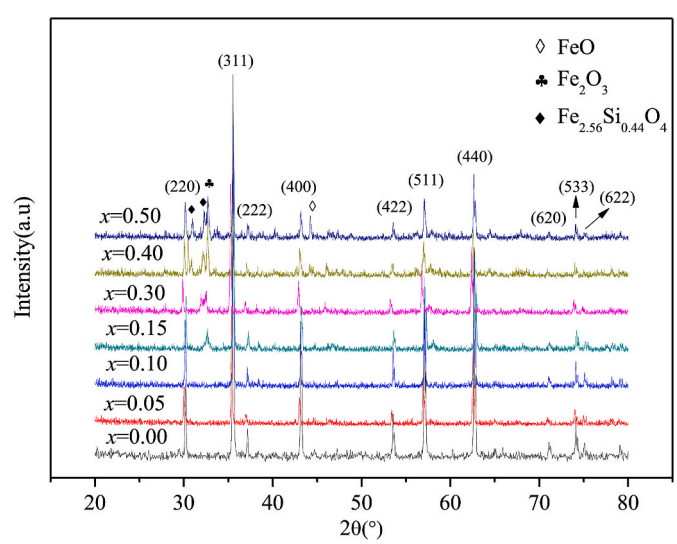


**Fig. 1.** XRD spectrum of $Si_xCo_{1-x}Fe_2O_4$ ferrites.

0.15, 0.30, 0.40, 0.50) ferrite with $x$ substitution are depicted in Fig. 1. As shown in Fig. 1, the inflection peak matches well with that of spinel within the error range when $0 \leq x < 0.15$; When $0.15 \leq x \leq 0.50$, $Fe_{2.56}Si_{0.44}O_4$, $Fe_2O_3$ and FeO heterophases appear in the diffraction pattern. This may be due to the balance of chemical valence, the replacement of $Si^{4+}$ ions make a part of the $Fe^{3+}$ ions change into $Fe^{2+}$ ions. Furthermore, the excessive substitution of $Si^{4+}$ makes $Si^{4+}$ ions fail to enter the spinel structure completely, thus forming impurity phases.

Table 2 shows the change of lattice parameters, theoretical density, X-ray density and porosity of the $Si_xCo_{1-x}Fe_2O_4$ ferrite with the substitution amount of silicon atom. The relationship among these parameters is given by formula (1), (2) and (3) in the experimental part. Derya Erdem et al. reports that $Si^{4+}$ has a strong preference for A-sites [7], so when $Si^{4+}$ takes the place of $Co^{2+}$, $Si^{4+}$ will occupy A-sites first, and squeeze the original $Fe^{3+}$ on A-positions to B-positions. Due to the equilibrium of chemical valence, part of $Fe^{3+}$ will change into $Fe^{2+}$ when Si takes the place of $Co^{2+}$. The radii of $Si^{4+}$, $Co^{2+}$, $Fe^{3+}$ and $Fe^{2+}$ are 0.4 Å, 0.82 Å, 0.67 Å, 0.83 Å, respectively. Therefore, as we can see from Table 2, the increase of lattice parameter ($a$) when $0 \leq x \leq 0.05$ may be due to the fact that a small amount of $Si^{4+}$ entered the lattice, which results in part of the small radius $Fe^{3+}$ transformed into the large radius $Fe^{2+}$. However, the lattice constant decreased when $0.05 < x \leq 0.15$ may be because the small radius $Si^{4+}$ (0.4 Å) replaces the large radius $Co^{2+}$ (0.82 Å), the $Si^{4+}$ enters the tetrahedral position. When $0.15 < x \leq 0.30$, the lattice constant increased again due to the formation of $Fe_{2.56}Si_{0.44}O_4$ heterophases at the grain boundary. $Si^{4+}$ does not enter the lattice completely, while $Fe^{2+}$ continues to increase, so the lattice continues to expand. Finally, when $0.30 < x \leq 0.50$, the decrease of lattice constant may be due to the excessive $Si^{4+}$ enters octahedral position in large quantities.

According to formula (2), with the increase of silicon substitution, the X-ray density reduced from 5.29 g/cm$^3$ to 4.94 g/cm$^3$. This phenomenon is largely thanks to the substitution of $Si^{4+}$ ions with lower relative atomic weight (28) for $Co^{2+}$ ions with higher relative atomic weight (58.93), resulting in the decrease of relative molecular weight, and it caused the X-ray density decrease.

### 3.2. Microstructure properties

The fracture surface morphologies of $Si_xCo_{1-x}Fe_2O_4$ ferrites with the different value of $x$ is depicted in Fig. 2. From (a) to (g), the porosity of the samples increased gradually, the grain size also increased slightly, besides the agglomeration between particles is deepened. This phenomenon indicates that the addition of silicon changed the microstructure of the samples. As far as we know, this kind of agglomeration may be thanks to changing distribution of magnetic ions at A and B positions by the addition of $Si^{4+}$, which is caused by the interaction among the magnetic ions [35]. Moreover, with the substitution of $Co^{2+}$ by $Si^{4+}$, in order to keep the charge equilibrium, the amount of metal ion vacancy closed to the grain boundary increases, which promotes the crystal boundary move, so the grain size increases [36].

As we can see from Table 2, the sintering density of the samples decreased with the improvement of $Si^{4+}$ ions substitution, which could result in the increase of porosity according formula (3). This is consistent with the increasing trend of porosity observed in Fig. 2.

**Table 2**
Structure parameters of $Si_xCo_{1-x}Fe_2O_4$ ferrites with $x$.

| x | $a$ (nm) | $d$ (g/cm$^3$) | $d_x$ (g/cm$^3$) | $P$ (%) |
|---|---|---|---|---|
| 0.00 | 0.8381 | 4.82 | 5.29 | 8.91 |
| 0.05 | 0.8401 | 4.65 | 5.22 | 10.90 |
| 0.10 | 0.8382 | 4.32 | 5.22 | 17.37 |
| 0.15 | 0.8369 | 4.52 | 5.21 | 13.34 |
| 0.30 | 0.8423 | 3.72 | 5.01 | 25.72 |
| 0.40 | 0.8395 | 3.62 | 4.99 | 27.48 |
| 0.50 | 0.8382 | 3.42 | 4.94 | 30.78 |

### 3.3. Magnetic performances

Fig. 3. (a) is the hysteresis loop diagram of $Si_xCo_{1-x}Fe_2O_4$ ferrites measured at normal atmospheric temperature. The variations of coercive force ($H_c$) and saturation magnetization ($M_s$) with the substitution amount of $Si^{4+}$ ions are shown in Fig. 3. (b). As is shown in Fig. 3. (b), the saturation magnetization ($M_s$) initially reduces when $x \leq 0.40$, and then improves when $x = 0.50$ with the improvement of Si substitution. On the other hand, the coercive force increases with the increasing substitution amount of $Si^{4+}$ ions on the whole.

Since cobalt ferrite is anti-spinel structure [11] and $Si^{4+}$ ions prefer to occupy A site [7], the metal ion distribution of $Si_xCo_{1-x}Fe_2O_4$ can be written in the following form:

$$\left(Si_x^{4+}Fe_{1-x}^{3+}\right)\left[Fe_x^{2+}Co_{1-x}^{2+}Fe^{3+}\right]O_4$$

The magnetic moments of $Si^{4+}$, $Co^{2+}$, $Fe^{2+}$ and $Fe^{3+}$ ions are 0, 3, 4 and 5 $\mu_B$. So, according to formula (6) and (7), the molecular magnetic moment of the sample can be calculated: $M = |6x + 3|$, and $M_s \propto M$, Therefore, theoretically, $M_s$ should increase with the increase of $x$. This is just in contradiction with the $M_s$ curve shown in Fig. 3 (b). The reason for this phenomenon may be the influence of porosity and impurities on the sample is the main factor.

Research findings that the magnetic performances of ferrite are closely related to its structure, composition, defect, internal stress and cation distribution [37]. In addition, the grain size and phase pureness of the sample also play an important role in the magnetic performances [38]. It may be noted that the saturated magnetization ($M_s$) and coercive force ($H_c$) of $CoFe_2O_4$ ferrite are largely decided by the cations distribution, particle size and shape of the grains [39].

When $0 \leq x < 0.10$, the saturated magnetization ($M_s$) is inversely proportional to the silicon content. This phenomenon can be explained from the following two aspects. For one thing, the superexchange interaction between atoms in A-B position is weakened as $Si^{4+}$ enters A-position, which result in the reduction of saturation magnetization ($M_s$); For another, because of the inverse relationship between porosity and magnetization of ferrite, the decrease of density and the increase of porosity also result in the reduction of saturation magnetization ($M_s$) [40]. When $0.10 < x \leq 0.40$, the reduction of saturation magnetization ($M_s$) can also be explicated by the interaction between A-B positions and porosity. Besides, the formation of impurity phase ($Fe_2O_3$ and $Fe_{2.56}Si_{0.44}O_4$) is also an important account for the decrease of saturation magnetization ($M_s$). Because the formation of secondary phase will increase the internal stress of the material, which will result in the reduce of saturation magnetization ($M_s$). when $0.40 < x \leq 0.50$, the change of saturation magnetization ($M_s$) is not obvious.

The coercive force ($H_c$) of $Si_xCo_{1-x}Fe_2O_4$ ferrites as a variable of $Si^{4+}$ substitution ($x$) is shown in the blue line in Fig. 3. (b), which suggests that $H_c$ increases in general with the improvement of the Si content. When $0 \leq x \leq 0.10$, the coercive force ($H_c$) of the samples improved sharply with the increase of Si substitution.

According to formula (4), the improvement of $H_c$ is mainly thanks to the reduce of $M_S$. In addition, according to the principle of magneto-crystalline anisotropy model, stress anisotropy and impurity model under multi-domain wall structure, $H_c$ improved with the improvement of magneto-crystalline anisotropy energy, stress, impurities contents and the reduce of $M_s$ [31]. Subsequently, the coercive force ($H_c$) increase slowly when $0.10 < x \leq 0.50$, which may be due to the formation of impurity phases. These newly formed phases increase the internal stress of the material. Fig. 2 indicates that the porosity of the samples is improving with the raise of Si concentration when $0.10 < x \leq 0.50$. Therefore, the increase of porosity is another account for the increasing coercive force.

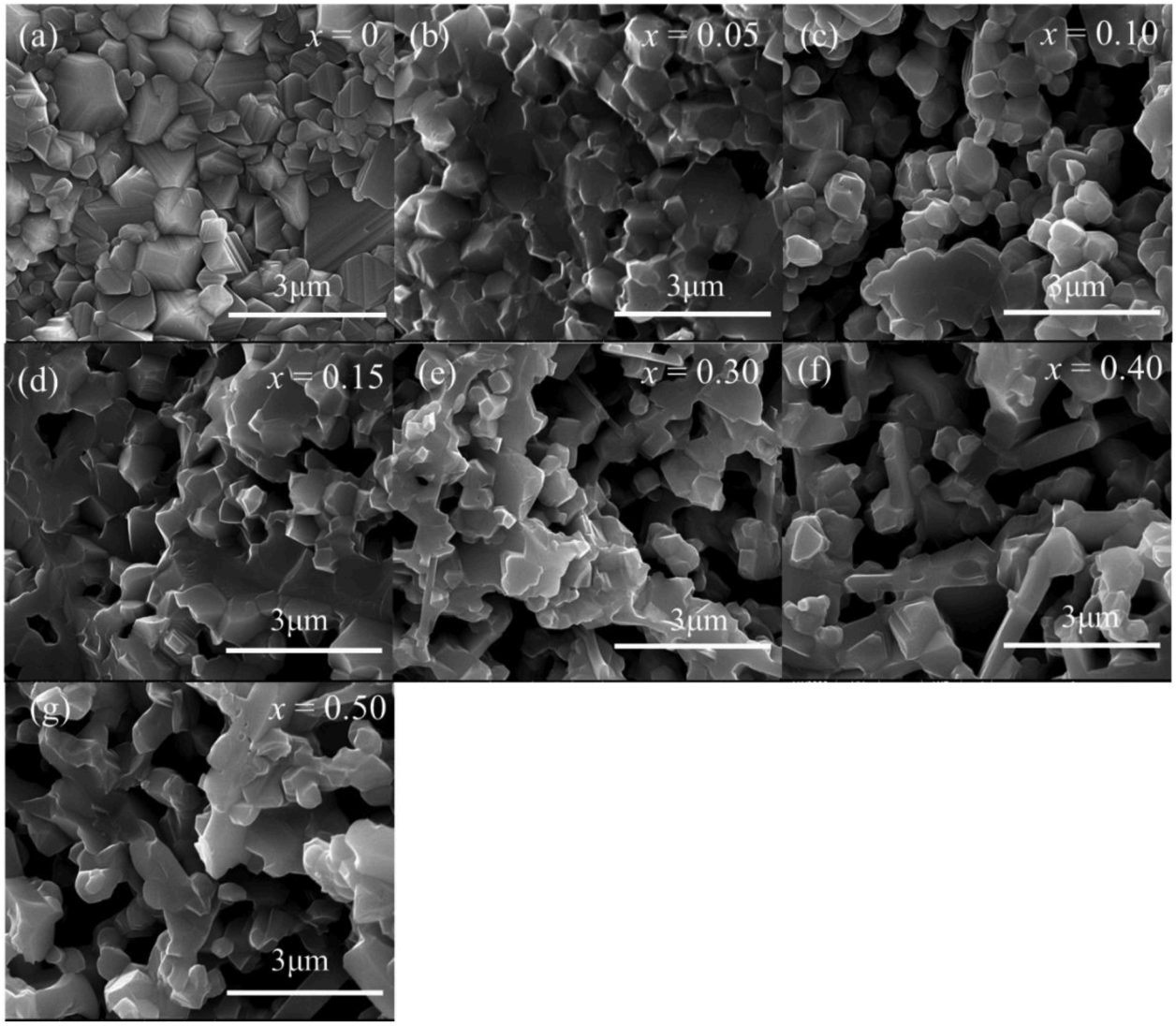


**Fig. 2.** SEM images of $Si_xCo_{1-x}Fe_2O_4$ ferrites.

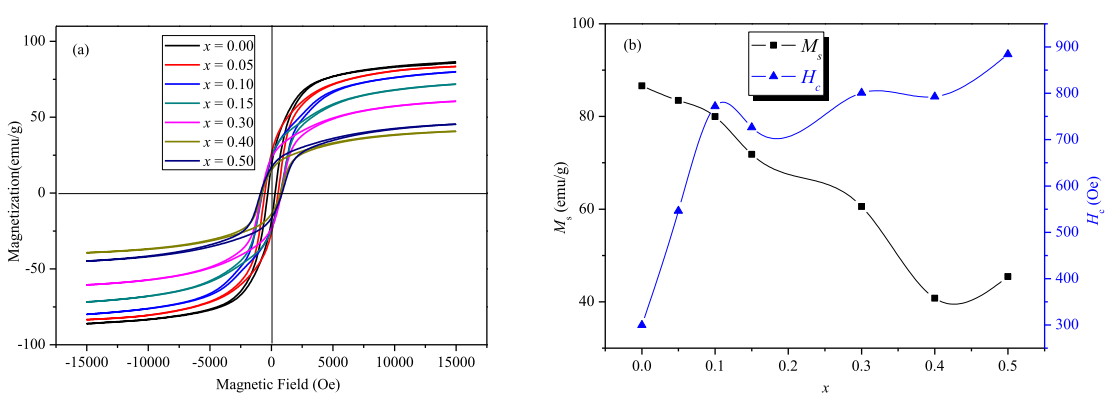


**Fig. 3.** (a) Hysteresis loops of $Si_xCo_{1-x}Fe_2O_4$ ferrites and (b) $M_s$ and $H_c$ of $Si_xCo_{1-x}Fe_2O_4$ ferrites.

### 3.4. Electrical performances

#### 3.4.1. The electrical conductivity

Fig. 4 (a-b) demonstrates the change curve of direct-current resistivity ($\rho_d$) with temperature for $Si_xCo_{1-x}Fe_2O_4$ ferrites. Fig. 4. (c) depicts the relationship between the activation energy ($E_\rho$) of the sample and the amount of Si substitution ($x$). We can see from this graph that the activation energy initially reduced and then improved with the raise of $x$, and there is a minimum when $x = 0.30$.

As a whole, the resistivity of the investigated samples reduces exponentially with the improvement of temperature expect the sample $x = 0.10$, which indicates they showed semiconductor characteristics.

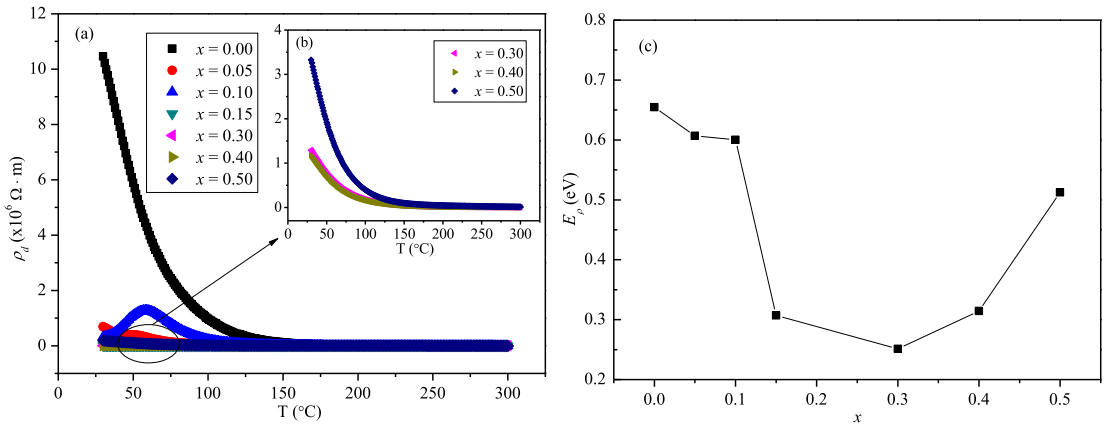


**Fig. 4.** (a) $\rho_d$ of the $Si_xCo_{1-x}Fe_2O_4$ ferrites ($x = 0$, 0.05, 0.10, 0.15, 0.30, 0.40, 0.50), (b) $\rho_d$ of the $Si_xCo_{1-x}Fe_2O_4$ ferrites ($x = 0.30$, 0.40, 0.50) and (c) $E_\rho$ of the $Si_xCo_{1-x}Fe_2O_4$ ferrites.

The sample with $x = 0.10$ indicats the metal-semiconductor transition behavior, it has a transition temperature $T_p$. When the temperature is below $T_p$, $\rho_d$ shows the metallic conduction performance and improved with the temperature; When the temperature is above $T_p$, $\rho_d$ displays the semi-conduction feature. The mechanism of metal conduction and semiconductor conduction as well as the transition temperature of ferrite have been studied [41,42]. The conductivity of ferrite is largely contributed to the diversion of electrons between $Fe^{2+}$ and $Fe^{3+}$ ions ($Fe^{2+} \leftrightarrow Fe^{3+} + e^-$) [43]. The electron diversions are decided by the activation energy [44]. The temperature dependence of direct-current resistivity ($\rho_d$) could be characterized by the formula: $\rho_d = \rho_0 \exp(E_\rho / kT)$ [45]. Where $\rho_0$ is the resistivity at at infinite temperature, $k$ is the Boltzman's constant. The activation energy ($E_\rho$) of ferrite with semi-conducting behavior can be concluded from the formula [46]. We can see that $\rho_d$ initially decreases when $0 \le x \le 0.30$ from Fig. 4 (a-b). As has been said above, $Fe^{2+}$ ions must be improving with the rise of $Si^{4+}$ contents. So the electron transfer between $Fe^{2+}$ and $Fe^{3+}$ is intensified and then it caused the decrease of $\rho_d$. Due to the increase of activation energy when $0.30 < x \le 0.50$, the potential barrier will increase, which will make it difficult to transfer electrons, increase the dc resistivity from Fig. 4. (c). So, the resistivity of the sample increased when $0.30 < x \le 0.50$.

### 3.4.2. The dielectric performances

Fig. 5 (a) and (b) depicts the dependence of the dielectric constant ($\varepsilon'$) of $Si_xCo_{1-x}Fe_2O_4$ ferrites in a frequency scale from 100 Hz to 1 MHz at normal atmospheric temperature.

Fig. 5 indicates that the dielectric constant ($\varepsilon'$) of all of the $Si_xCo_{1-x}Fe_2O_4$ ferrites decrease exponentially with the increase of frequency approximately. Ferrite materials are composed of grains with good conductivity, and there are grain boundaries with poor conductivity between the grains [47]. The large space charge polarization will be produced due to electrons gather at the grain boundary with high resistance [48]. Therefore, the dielectric constant value is large at low frequency. When the frequency exceeds a certain value, the electron diversion between $Fe^{2+}$ and $Fe^{3+}$ can't catch up with the change of

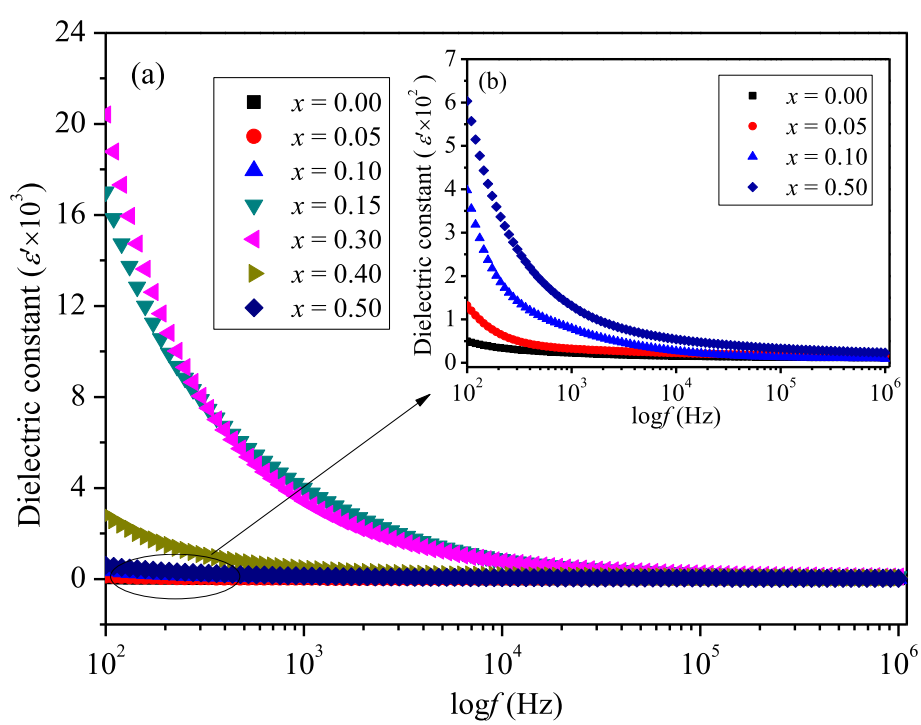


**Fig. 5.** (a) Dielectric constant of all the investigated $Si_xCo_{1-x}Fe_2O_4$ ferrites ($x = 0$, 0.05, 0.10, 0.15, 0.30, 0.40, 0.50) and (b) Dielectric constant $Si_xCo_{1-x}Fe_2O_4$ ferrites ($x = 0$, 0.05, 0.10, 0.50).

alternating electric field [49]. Therefore, their contribution to polarization will decrease dramatically. This is consistent with the fact that the actual permittivity is a low constant at high frequencies.

Besides, Fig. 5 shows that the dielectric constant ($\varepsilon'$) initial increases and then decreases with the amount of Si substitution, and reaching the peak when $x = 0.30$. The dielectric constant ($\varepsilon'$) increases with the increase of $x$ due to the increase of $Fe^{2+}$ in octahedral position when $0 \leq x < 0.30$. Because some research shows that the polarizability of ferrite depends on the local displacement of electrons between $Fe^{2+}$ and $Fe^{3+}$ in the outfield direction [37,50]. It is pointed out above that due to the addition of Si, in order to maintain the chemical valence balance, part of $Fe^{3+}$ will be converted to $Fe^{2+}$. Therefore, the number of $Fe^{2+}$ on octahedral position increases. When $0.30 < x \leq 0.50$, the dielectric constant ($\varepsilon'$) is inversely proportional to the value of $x$. This is because the resistivity improved with the improvement of $x$ value, which results in the reduction of space charge polarization, so the dielectric constant decreases [51].

## 4. Conclusion

In this paper, the effect of silicon substitution on the electromagnetic properties of cobalt ferrite ($Si_xCo_{1-x}Fe_2O_4$ where $x = 0, 0.05, 0.10, 0.15, 0.30, 0.40, 0.50$) was studied. Among them, the substitution amount of silicon has an important influence on the microstructure and electromagnetic performance of the samples. According to XRD, the structure of the prepared sample is single-phase when $x < 0.15$, while the impurity phase $Fe_2O_3$, $Fe_{2.56}Si_{0.44}O_4$ and FeO appeared in the prepared sample when $x \geq 0.15$. According to SEM, the grain size and porosity of the samples increase with the increase of $Si^{4+}$ substitution, which shows that the addition of $Si^{4+}$ improves the microstructure of cobalt ferrite. According to VSM, the addition of silicon decreases the saturated magnetization ($M_s$) of the sample, but its coercive force ($H_c$) increases. In addition, the substitution of silicon for cobalt also improves the dc resistivity of cobalt ferrite. When $x = 0.30$, the dc resistivity of the sample reaches the minimum. Finally, the real dielectric coefficient $\varepsilon'$ of the investigated samples initial improve when $x \leq 0.30$, then reduce when $x > 0.30$. This indicates that the dielectric properties of cobalt ferrite are greatly improved by adding silicon.

## Declaration of competing interest

The authors declare no conflict of interest.

## Acknowledgments

This work was supported by the Project of Science and Technology Supporting Plan in Sichuan Province of China (2019YJ0354, 2019YJ0364), the National Natural Science Foundation of China Grant (51701025) and Research Found for Young Academic Leaders of CUIT Grant (J201710).

## References

[1] R. Kumar, M. Kar, Lattice strain induced magnetism in substituted nanocrystalline cobalt ferrite, J. Magn. Magn Mater. 416 (2016) 335–341.
[2] P.K. Chougule, S.S. Kumbhar, Y.D. Kolekar, C.H. Bhosale, Enhancement in curie temperature of nickel substituted Co–Mn ferrite, J. Magn. Magn Mater. 372 (2014) 181–186.
[3] B.G. Toksha, S.E. Shirsath, M.L. Mane, K.M. Jadhav, Auto-ignition synthesis of $CoFe_2O_4$ with $Al^{3+}$ substitution for high frequency applications, Ceram. Int. 43 (2017) 14347–14353.
[4] T. Dipponga, D. Tolomanb, E.A. Leveic, O. Cadarc, A. Mesaros, A possible formation mechanism and photocatalytic properties of $CoFe_2O_4$/PVA-$SiO_2$ nanocomposites, Thermochim. Acta 666 (2018) 103–115.
[5] T. Dipponga, O. Cadarb, E.A. Leveib, I.G. Deacc, G. Borodi, Formation of $CoFe_2O_4$/PVA-$SiO_2$ nanocomposites: effect of diol chain length on the structure and magnetic properties, Ceram. Int. 44 (2018) 10478–10485.
[6] T. Dipponga, O. Cadarb, E.A. Leveib, I.G. Deacc, F. Gogad, G. Borodie, L. B. Tudoran, Influence of polyol structure and molecular weight on the shape and properties of $Ni_{0.5}Co_{0.5}Fe_2O_4$ nanoparticles obtained by sol-gel synthesis, Ceram. Int. 45 (2019) 7458–7467.
[7] D. Erdem, N.S. Bingham, F.J. Heiligtag, N. Pilet, P. Warnicke, L.J. Heyderman, M. Niederberger, $CoFe_2O_4$ and $CoFe_2O_4$-$SiO_2$ nanoparticle thin films with perpendicular magnetic anisotropy for magnetic and magneto-optical applications, Adv. Funct. Mater. 26 (2016) 1954–1963.
[8] M.A. Almessiere, Y. Slimani, S. Güner, M. Nawaz, A. Baykal, F. Aldakheel, S. Akhtar, I. Ercan, İ. Belenli, B. Ozçelik, Magnetic and structural characterization of $Nb^{3+}$-substituted $CoFe_2O_4$ nanoparticles, Ceram. Int. 45 (2019) 8222–8232.
[9] T. Dippong, E.A. Levei, O. Cadar, F. Goga, D. Toloman, G. Borodi, Thermal behavior of Ni, Co and Fe succinates embedded in silica matrix, J. Therm. Anal. Calorim. 136 (2019) 1587–1596.
[10] T. Dippong, E.A. Levei, O. Cadar, Preparation of $CoFe_2O_4$/$SiO_2$Nanocomposites at low temperatures using short chain diols, J. Chem. 2017 (2017) 1–11.
[11] T. Dipponga, O. Cadarb, E.A. Leveib, I.G. Deacc, L. Diamandescud, L.B. Tudoran, Influence of cobalt ferrite content on the structure and magnetic properties of $(CoFe_2O_4)_x(SiO_2\text{-}PVA)_{100-x}$ nanocomposites, Ceram. Int. 44 (2018) 7891–7901.
[12] T. Dipponga, E.A. Leveib, I.G. Deacc, F. Gogad, O. Cadarb, Investigation of structural and magnetic properties of $Ni_xZn_{1-x}Fe_2O_4$/$SiO_2$ ($0 \leq x \leq 1$) spinel-based nanocomposites, J. Anal. Appl. Pyrolysis 144 (2019) 104713–104725.
[13] T. Dippong, O. Cadar, E.A. Levei, I.G. Deac, Microstructure, porosity and magnetic properties of $Zn_{0.5}Co_{0.5}Fe_2O_4$/$SiO_2$ nanocomposites prepared by sol-gel method using different polyols, J. Magn. Magn Mater. 498 (2020) 166168–166191.
[14] P.S. Das, G.P. Singh, Structural, Magnetic and dielectric study of Cu substituted NiZn ferrite nanorod, J. Magn. Magn Mater. 401 (2016) 918–924.
[15] M. De, S. Bera, H.S. Tewari, Structural characterization of magnesium-substituted nickel ferrite nanoparticles, Emerg. Mater. Res. 6 (2017) 265–269.
[16] S. Kumar, S. Munjal, N. Khare, Metal-semiconductor transition and seebeck inversion in $CoFe_2O_4$ nanoparticles, J. Phys. Chem. Solid. 105 (2017) 86–89.
[17] S.A. Mazen, A.M. El Taher, The conduction mechanism of Cu–Si ferrite, J. Alloys Compd. 498 (2010) 19–25.
[18] S.S. Shinde, K.M. Jadhav, Electrical and dielectric properties of silicon substituted cobalt, Mater. Lett. 37 (1998) 63–67.
[19] M. Mozaffari, J. Amighian, Preparation of Al-substituted Ni ferrite powders via mechanochemical processing, J. Magn. Magn Mater. 260 (2003) 244–249.
[20] D.R. Mane, U.N. Devatwal, K.M. Jadhav, Structural and magnetic properties of aluminium and chromium Co-substituted cobalt ferrite, Mater. Lett. 44 (2000) 91–95.
[21] H.H. Joshi, R.G. Kulkarni, Mössbauer study of the spinel system $Ti_xCo_{1+x}Fe_{2-2x}O_4$, Solid State Commun. 60 (1) (1986) 67–69.
[22] A. Lassoued, J.F. Li, Magnetic and photocatalytic properties of Ni–Co ferrites, Solid State Sci. 104 (2020) 106199–106241.
[23] S.E. Shirsath, B.G. Toksha, K.M. Jadhav, Structural and magnetic properties of $In^{3+}$ substituted $NiFe_2O_4$, Mater. Chem. Phys. 117 (2009) 163–168.
[24] H. Yu, Z.J. Zhang, L. Guo, Theoretical study on cobalt ferrite $Co_nFe_{3-n}O_4$ (n=1–2) nanoparticles with multi-enzyme activities, Catal. Surv. Asia 24 (2020) 166–177.
[25] H.H. Joshi, R.B. Jotania, R.G. Kulkarni, Fe mossbauer and magnetic studies on the spinel system $Co_{1+x}Ge_xFe_{2\text{-}2x}$, Solid State Commun. 78 (1991) 539–542.
[26] S.A. Mazen, N.I. Abu-Elsaad, A.S. Nawara, Influence of silicon substitution and annealing temperature on the microstructure and magnetic properties of lithium ferrite, J. Alloys Compd. 648 (2015) 690–697.
[27] O.V. Merkulov, A.A. Markov, M.V. Patrakeev, A.V. Chukin, I.A. Leonidov, V. L. Kozhevnikov, Structural features and high-temperature properties of $SrFe_{1-x}Si_xO_{3-\delta}$, Solid State Ionics 292 (2016) 83–87.
[28] H. Yamahara, M. Seki, H. Tabata, High temperature spin cluster glass behavior in Co- and Si-substituted garnet ferrite thin films, J. Magn. Magn Mater. 501 (2020) 166437–166475.
[29] N. Ranvah, I.C. Nlebedim, Y. Melikhov, J.E. Snyder, D.C. Jiles, A.J. Moses, P. I. Williams, F. Anayi, S.H. Song, Temperature dependence of magnetostriction of $Co_{1+x}Ge_xFe_{2\text{-}2x}O_4$ for magnetostrictive sensor and actuator applications, IEEE Trans. Magn. 44 (2008) 3013–3016.
[30] L.Z. Li, Z. Yu, Z.W. Lan, K. Sun, C.J. Wu, Structural and magnetic properties of Mg-substituted NiZnCo ferrite nanopowders, Ceram. Int. 40 (2014) 13917–13921.
[31] S. Amiri, H. Shokrollahi, Magnetic and structural properties of RE doped Co-ferrite (RE = Nd, Eu, and Gd) nano-particles synthesized by co-precipitation, J. Magn. Magn Mater. 345 (2013) 18–23.
[32] E.R. Kumar, R. Jayaprakash, S. Kumar, Effect of annealing temperature on structural and magnetic properties of manganese substituted $NiFe_2O_4$ nanoparticles, Mater. Sci. Semicond. Process. 17 (2014) 173–177.
[33] Ş. Kuru Tuğba, Room temperature structural, dielectric, and conductivity properties of $Al_xCd_{1-x}Fe_2O_4$ ferrites, J. Australas. Ceram. Soc. 56 (2019) 453–460.
[34] L.Z. Li, L. Peng, X.X. Zhong, R. Wang, X.Q. Tu, Structural and magnetic properties of strontium substituted NiZn ferrite nanopowders, Ceram. Int. 42 (2016) 13238–13241.
[35] N.T.T. Loan, N.T.H. Lan, N.T.T. Hang, N.Q. Hai, D.T.T. Anh, V.T. Hau, L.V. Tan, T. V. Tran, $CoFe_2O_4$ nanomaterials: effect of annealing temperature on characterization, magnetic, photocatalytic, and photo-fenton properties, Processes 7 (2019) 885–899.
[36] Z.Q. Liu, Z.J. Peng, C.C. Lv, X.L. Fu, Doping effect of $Sm^{3+}$ on magnetic and dielectric properties of Ni-Zn ferrites, Ceram. Int. 43 (2017) 1449–1454.
[37] L.Z. Li, X.X. Zhong, R. Wang, X.Q. Tu, L. He, R.D. Guo, Z.Y. Xu, Structural, magnetic and electrical properties in Al-substitued NiZnCo ferrite prepared via the sol–gel auto-combustion method for LTCC technology, RSC Adv. 7 (2017) 39198–39203.

[38] T. Prabhakaran, R.V. Mangalaraja, J.C. Denardin, J.A. Jimenez, The effect of calcination temperature on the structural and magnetic properties of Co-precipitated $CoFe_2O_4$ nanoparticles, J. Alloys Compd. 716 (2017) 171–183.
[39] S. Javadi, S.M. Masoudpanah, A. Zakeri, Conventional versus microwave combustion synthesis of $CoFe_2O_4$ nanoparticles, J. Sol. Gel Sci. Technol. 79 (2016) 176–183.
[40] M. Kaiser, Effect of rare earth elements on the structural, magnetic and electrical behavior of Ni-Zn-Cr nanoferrites, J. Alloys Compd. 719 (2017) 446–454.
[41] L.Z. Li, X.X. Zhong, R. Wang, X.Q. Tu, L. He, Effects of Al substitution on the properties of NiZnCo ferrite nanopowders, J. Mater. Sci. Mater. Electron. 29 (2018) 7233–7238.
[42] L. Peng, L.Z. Li, X.X. Zhong, Y. Hu, X.Q. Tu, R. Wang, Magnetic, electrical, and dielectric properties of La-Cu substitued Sr-hexaferrites for use in microwave LTCC devices, J. Alloys Compd. 665 (2016) 31–36.
[43] E.J.W. Verwey, J.H. De Boer, Cation arrangement in a few oxides with crystal structures of the spinel type, Recl. Trav. Chim. Pays-Bas 55 (1936) 531–540.
[44] A. Lakshman, P.S.V.S. Rao, B.P. Rao, et al., Electrical properties of $In^{3+}$ and $Cr^{3+}$ substituted magnesium–manganese ferrites, J. Phys. D 38 (2005) 673–678.
[45] U.V. Chhaya, R.G. Kulkarni, Metal-insulator type transition in aluminium and chromium co-substituted nickel ferrites, Mater. Lett. 39 (1999) 91–96.
[46] A. Thakur, P. Mathur, M. Singh, Study of dielectric behaviour of Mn–Zn nano ferrites, J. Phys. Chem. Solid. 68 (2007) 378–381.
[47] M.N. Slam, A.K.M.A. Hossain, Enhancement of Néel temperature and electrical resistivity of Mn–Ni–Zn ferrites by $Gd^{3+}$ substitution, J. Mater. Res. Technol. 8 (2019) 208–216.
[48] B.B.V.S. V Prasad, B.R. Babu, M.S.R. Prasad, Structural and dielectric studies of $Mg^{2+}$ substituted Ni–Zn ferrite, Mater. Sci.-Poland 33 (2015) 806–815.
[49] S. Hussain, M. Anis-ur-Rehman, A. Maqsood, M.S. Awan, The effect of $SiO_2$ addition on structural, magnetic and electrical properties of strontium hexa-ferrites, J. Cryst. Growth 297 (2006) 403–410.
[50] M. Naeem, N.A. Shah, I.H. Gul, A. Maqsood, Structural, electrical and magnetic characterization of Ni–Mg spinel ferrites, J. Alloys Compd. 487 (2009) 739–743.
[51] H.I. Hsiang, L.T. Mei, C.S. His, Y.L. Liu, F.S. Yen, Electrical properties of low temperature sintered copper and titanium-codoped copper zinc ferrites, J. Alloys Compd. 502 (2010) 163–168.